Adjustment of the Remote Tropical Climate to El Niño Conditions

BENJAMIN R. LINTNER* AND JOHN C. H. CHIANG

Department of Geography, and Berkeley Atmospheric Sciences Center, University of California, Berkeley, Berkeley, California

(Manuscript received 13 January 2006, in final form 23 October 2006)

ABSTRACT

The adjustment of the tropical climate outside the Pacific (the "remote Tropics") to the abrupt onset of El Niño conditions is examined in a tropical atmosphere model that assumes simplified vertical structure and quasi-equilibrium (QE) convective closure. The El Niño signal is rapidly (~1 week) communicated to the remote Tropics via an eastward-propagating Kelvin-like wave that induces both anomalous subsidence and tropospheric warming. Widespread reductions in convective precipitation occur in conjunction with the spreading of the temperature and subsidence anomalies. The remote rainfall suppression peaks roughly 5–15 days after the initiation of El Niño conditions, after which the anomalous remote rainfall field recovers to a state characterized by a smaller remote areal mean rainfall deficit and the appearance of localized positive rainfall anomalies. The initial remote precipitation reduction after El Niño onset is tied to both tropospheric warming (i.e., stabilization of the troposphere to deep convection) and the suppression of remote humidity levels; recovery of the initial deficits occurs as feedbacks modulate the subsequent evolution of humidity anomalies in the tropospheric column. Apart from the short-term response, there is a longer-term adjustment of the remote climate related to the thermal inertia of the underlying surface: surface thermal disequilibrium, which is related to the depth of the ocean mixed layer, maintains larger precipitation deficits than would be expected for equilibrated conditions. This result supports a previous prediction by one of the authors for a significant disequilibrium mechanism in the precipitation teleconnection to El Niño resulting from the local vertical coupling of the troposphere to the surface through moist convection.

1. Introduction

During El Niño–Southern Oscillation (ENSO) events, substantial climate anomalies occur throughout the Tropics outside of the Pacific source region (hereafter, the "remote Tropics"). Warm sea surface temperature (SST) anomalies in the eastern equatorial Pacific drive convective heating anomalies that in turn cause remote tropical changes through a suite of teleconnected dynamical and thermodynamic linkages, commonly referred to as the atmospheric bridge (Lau and Nath 1996; Klein et al. 1999). The foundation of the atmospheric bridge is that anomalous forced ascent over the Pacific is balanced by compensatory descent elsewhere, as suggested by the simple shallow water model of Gill (1980). More recent studies (Alexander et al. 2002; Giannini et al. 2001; Su et al. 2001; Chiang and Sobel 2002, hereafter CS02; Su and Neelin 2002; Chiang and Lintner 2005; Lintner and Chiang 2005; Neelin and Su 2005) have refined and augmented the Gill picture by considering more realistic land–ocean–atmosphere interactions, moist convective dynamics, and inhomogeneous basic states. For example, CS02 emphasized the role of thermodynamics, particularly temperature, in propagating the ENSO signal to the remote Tropics. Su and Neelin (2002) and Neelin and Su (2005) focused on the role of regionally variable moisture-related processes (e.g., advection and evaporation) in mediating El Niño–related precipitation changes.

Although the atmospheric bridge represents the dominant conceptual framework of the ENSO teleconnection, relatively little attention has been devoted to

* Current affiliation: Department of Atmospheric and Oceanic Sciences, and Institute of Geophysics and Planetary Physics, University of California, Los Angeles, Los Angeles, California.

Corresponding author address: Dr. Benjamin R. Lintner, Department of Atmospheric and Oceanic Sciences, and Institute of Geophysics and Planetary Physics, 7127 Mathematical Sciences Building, University of California, Los Angeles, Los Angeles, CA 90095-1565.
E-mail: ben@atmos.ucla.edu

DOI: 10.1175/JCLI4138.1

its transient characteristics. The use of monthly mean and longer-term anomalies—the typical basis of ENSO teleconnection studies—emphasizes climatic conditions after adjustment to ENSO forcing has largely occurred. However, monthly (or longer) averages do not reveal how the anomalies come about in the first place. Thus, we adopt here a different approach: we examine the transient evolution of remote tropical climate anomalies after the sudden introduction of peak El Niño conditions.

Since the time evolution of observed ENSO events is slow compared to the rapid adjustment time scales of the tropical atmosphere, the abrupt onset framework may not be strictly comparable to the observed teleconnection. Nevertheless, we show that the short-term transient evolution to abrupt El Niño onset offers valuable insight into the mechanisms underlying the teleconnection. For example, a central finding of our study is the dominance of equatorial, Kelvin-like wave dynamics in the communication of the initial ENSO signal to the remote Tropics. Following the initial wave dynamical impact, significant feedbacks modulate the remote climatic response. The interplay of initial impacts and feedbacks would be difficult to discern in the static paradigm.

Apart from the fast atmospheric adjustment, there are adjustment effects associated with more slowly responding ocean and, possibly, land components of the climate system. CS02 argued that the El Niño phase precipitation deficits occurring over the remote tropical oceans may be partially attributed to a thermal disequilibrium effect: the tropical tropospheric warming induced by El Niño causes the underlying ocean surface to warm, but with a temporal lag corresponding to the ocean thermal inertia. The resulting surface flux disequilibrium reduces (for example) evaporation from the ocean to the atmosphere and hence reduces precipitation. Tang and Neelin (2004) noted changes in tropical Atlantic cyclogenesis, including hurricane intensity and frequency, that are strongly correlated to measures of the surface disequilibrium.

The principal objective of our study is to explore the range of adjustment effects associated with the onset of El Niño, using an intermediate level complexity model containing physics essential to the tropical teleconnection but also amenable to detailed analysis. After introducing the models and methodology in section 2, we document the principal features of the remote tropical adjustment, especially the precipitation response, as it occurs under abrupt El Niño onset (section 3). We distinguish two phases in the evolution of the remote climate anomalies: a rapid *initial phase* characterized by a propagating Kelvin-like wave influence from the tropical Pacific and widespread rainfall reduction over the remote Tropics and a slower *equilibrating phase* during which climate feedbacks modify the remote climate response, leading to a spatially complex equilibrated structure. Sections 4 and 5 explore the mechanisms responsible for the anomalous precipitation behavior during the initial phase and the subsequent transition to equilibrium. We also examine how the transition to equilibrium depends on surface thermal inertia effects.

2. Models and methodology

The Quasi-equilibrium Tropical Circulation Model 1 version 2.3 (QTCM1), the principal model used, is an intermediate-level complexity model of the tropical atmosphere (Neelin and Zeng 2000; Zeng et al. 2000). QTCM1 solves the primitive equations on a horizontal grid (here, $5.625° \times 3.75°$) while assuming fixed vertical structures especially tailored for tropical deep convection regions. The version used here has a single first-baroclinic mode for temperature, barotropic and first-baroclinic modes for horizontal momentum, and a single moisture mode that broadly resembles the vertical distribution of observed tropical moisture. Like a general circulation model, QTCM1 includes parameterizations of all relevant subgrid-scale physics including radiation, moist convection, and surface exchange processes. An important feature of QTCM1 is its reliance on quasi-equilibrium (QE) convective closure: the assumption that moist convection determines the tropical circulation constrains the vertical structure, with a Betts–Miller convective parameterization (Betts and Miller 1986) relaxing the actual temperature profile to a reference profile. The simplifications inherent to QTCM1 should be kept in mind when considering the results and their interpretation.

There are significant advantages to using QTCM1 for mechanistic studies, the most important of which is that it readily facilitates physically meaningful diagnoses with greater ease and flexibility than is possible with conventional general circulation models (GCMs). For example, it is straightforward to configure sensitivity experiments with one or more fields of interest fixed to climatology; we employ this approach here. QTCM1 has been used extensively in a diverse array of problems in tropical climate dynamics: along with its previous application to the study of tropical teleconnections, the model has been used to study monsoons (Chou et al. 2001), ocean–atmosphere coupling (Su et al. 2003, 2005), tropical climate sensitivity to global warming (Neelin et al. 2003; Chou and Neelin 2004; Neelin and Chou 2004), and land–atmosphere and vegetation–atmosphere interactions (Zeng and Neelin 1999, 2000; Zeng et al. 1999; Hales et al. 2004).

To lend credence to the QTCM1 results, comparisons are made to similar abrupt ENSO onset simulations from a full GCM, the National Center for Atmospheric Research (NCAR) Community Climate Model version 3.10 (or CCM3; see Kiehl et al. 1998 for a detailed description). The CCM3 simulations were performed at a horizontal resolution corresponding to triangular truncation with 31 basis functions in the meridional and 15 in the zonal, which is equivalent to 48 grid points in both longitude and latitude. In the vertical, the standard 18 sigma-hybrid levels were retained. While coarse, this resolution is adequate to simulate the tropical ENSO teleconnection at the spatial scales of interest (Chiang and Lintner 2005). The land surface component, Land Surface Model 1.0, a one-dimensional model for determining land surface energy, momentum, water, and carbon dioxide exchanges, is described in Bonan (1998).

Each model was forced with Pacific region peak El Niño SST anomalies (SSTAs) switched on at the beginning of the simulation and subsequently fixed. The imposed SSTAs, corresponding to January 1998, were derived from the National Centers fro Environmental Prediction (NCEP)–NCAR reanalysis SST dataset (Kalnay et al. 1996) and applied in the Pacific between 20°S and 20°N from 135°E to the western coastline of the Americas; the anomalies were linearly relaxed to zero over a 10° interval on the northern and southern margins of the forcing region and over a 25° interval on its western edge. To suppress the effects of seasonality, the background climate state (in the QTCM1 simulations only) was fixed to perpetual January mean state conditions; that is, the background SST field, top-of-the-atmosphere insolation, and surface albedo were set to their mean January values, unless otherwise stated. The constant SST forcing and perpetual January conditions simplify the time-evolving signatures of the remote tropical climate as it adjusts to equilibrium. Outside of the Pacific forcing region, the models were coupled at all ocean grid points to a thermodynamical slab ocean model with Q-flux adjustment to maintain a realistic SST climatology (Chiang et al. 2003). For most simulations analyzed, ensembles of 20 members were constructed, with each ensemble member integrated for 240 days; the analysis consists of ensemble mean averages unless otherwise stated.

3. Transient adjustment to abrupt ENSO onset

a. Abrupt ENSO onset in CCM3

We first consider daily snapshots of remote tropical climate anomalies immediately after El Niño onset (Fig. 1). The vertically averaged tropospheric temperature field (first row) shows rapid eastward progression of warming between 20°N and 20°S subsequent to El Niño onset. Associated with the temperature wave front are anomalies in the horizontal velocity (u, v; second row), specific humidity (q; third row), and precipitation (P; fourth row). The copropagation of these anomalies underscores the rapid communication of ENSO-related climate signatures to the remote Tropics. The spatial characteristics of these anomalies resemble a Kelvin wave propagating along the equatorial waveguide (Gill 1980, 1982a,b; Heckley and Gill 1984; Neelin and Su 2005). The propagation speed of the wave front can be estimated by following the leading edge of the temperature anomalies, yielding a mean wave speed value of $\sim$20 m s^{-1} along the equator. It should be noted that this value is slow compared to the $\sim$45 m s^{-1} idealized shallow water model wave speed, assuming a 200-m equivalent depth appropriate to the first-baroclinic mode of the tropical troposphere. The difference in wave speeds between the dry shallow water model and CCM3 likely results from wave interaction with moist dynamics (Gill 1982a,b; Nakajima et al. 2004; Frierson 2007), a point to which we return later.

The upper-level circulation anomalies are part of the anomalous Walker circulation, which is frequently invoked in the linkage between the Pacific and remote tropical regions (Kidson 1975; Lau and Nath 1996; Klein et al. 1999; Saravanan and Chang 2000). Anomalous upper-level westerlies converge near the temperature wave front and imply, by continuity, midtropospheric subsidence and lower-level divergence. A near-surface easterly return flow (not shown) closes the circulation. The upper-level westerlies, low-level easterlies, and subsidence persist even after the passage of the temperature wave front. Based on a dry, uncoupled atmospheric model, Heckley and Gill (1984) argued that the transition to equilibrium (at a particular point) should occur on a time scale roughly equal to the longitudinal width of the heating region—effectively, the width of the Niño-3 region, or $\sim$60°—divided by the propagation speed, that is, 4 days. However, disequilibrium effects likely lengthen this adjustment time.

The initial development of precipitation anomalies along the leading edge of the temperature signal suggests control of the remote precipitation response by tropospheric temperature. The warming of the remote tropical troposphere effectively stabilizes the troposphere to deep convection, thereby decreasing rainfall. The column-integrated specific humidity decreases immediately after onset; however, the vertically averaged behavior belies a prominent vertical dipole, with midtropospheric humidity levels generally decreasing and boundary layer values increasing. Such behavior is

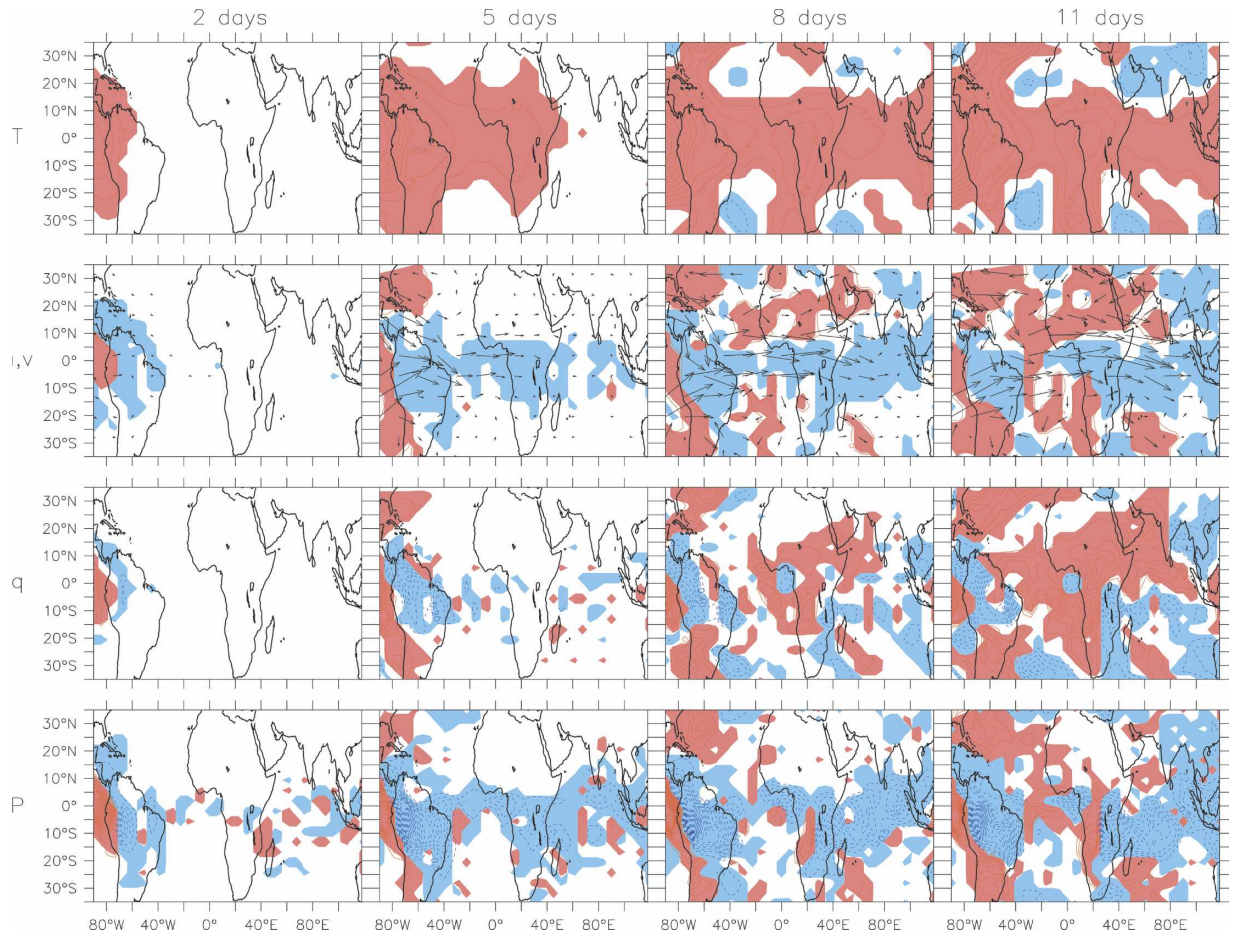

FIG. 1. Selected remote tropical field anomalies immediately after El Niño onset in NCAR CCM3. Plotted fields are (first row) vertically averaged tropospheric temperature (K), (second row) 200-mb horizontal wind components (vectors; m s^{-1}) with 500-mb vertical velocity (i.e., negative pressure velocity; blue shading is negative or downward and red is positive or upward), (third row) vertically averaged specific humidity (K), and (fourth row) precipitation (mm day^{-1}) for days 2, 5, 8, and 11 following abrupt El Niño onset. The predominance of the warm Kelvin wave in communicating the El Niño influence to the remote Tropics is evident, with the initial suppression of the remote tropical precipitation as a direct consequence.

broadly consistent with stabilization, as the subsiding air aloft dries the middle troposphere while reduced convection inhibits delivery of moisture from the boundary layer to the free troposphere, thereby increasing boundary layer moisture values.

b. Abrupt ENSO onset in QTCM1

Daily snapshots of the same quantities shown in Fig. 1 for CCM3 reveal a qualitatively comparable adjustment process occurring in QTCM1 (Fig. 2). A prominent eastward-propagating, tropical Kelvin-like wave of temperature and circulation anomalies is apparent (first and second rows), with an associated reduction in precipitation (fourth row). One point of departure between the CCM3 and QTCM1 results is the behavior of the vertically averaged specific humidity field (third row): for example, during day 5, widespread negative anomalies are present over South America in CCM3, but this region exhibits weakly negative or even positive anomalies in QTCM1. This difference directly reflects the single-mode vertical structure of humidity in QTCM1; by design, the vertical moisture basis function has its largest loading in the boundary layer, where humidity values in CCM3 increase soon after onset.

The speed of the QTCM1 temperature wave front is ~14 m s^{-1} along the equator, which, while somewhat slower than the wave speed estimated from the CCM3 data, is again much less than that expected for a dry shallow water model. This is not unexpected—the inclusion of moisture effectively decreases the static stability experienced by the wave, lowering the wave speed. For this reason, such waves are referred to as "moist Kelvin" or "convectively coupled" waves. Neelin and Yu (1994) performed an eigenvalue analysis for

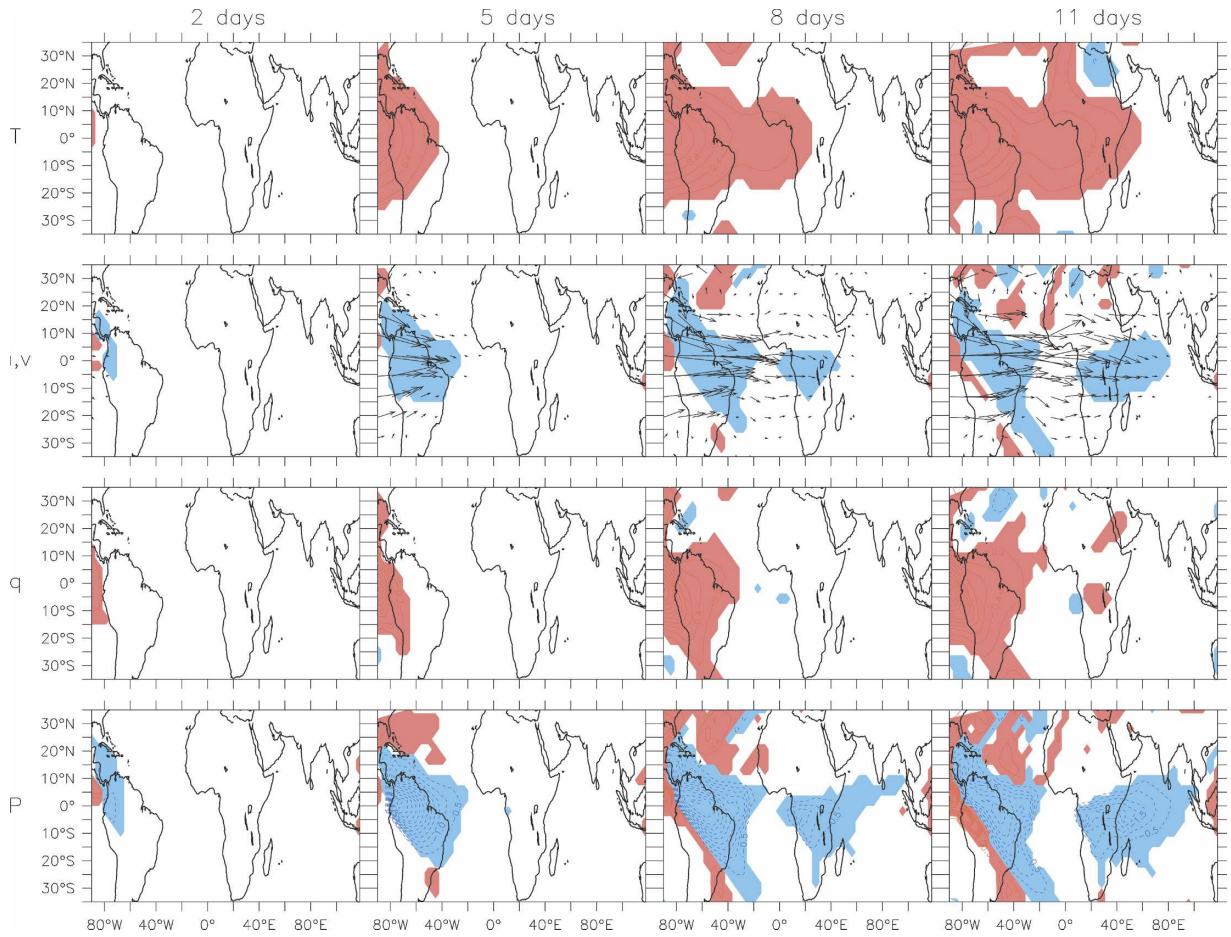

FIG. 2. Selected anomalies subsequent to abrupt El Niño onset in QTCM1. As in Fig. 1. The establishment of the QTCM1 response is qualitatively similar to that of the CCM3, although the Kelvin wave propagation is noticeably slower (because of the stronger coupling between the wave and moist processes in the QTCM1).

an idealized moist convective tropical atmosphere and obtained propagation speeds of order 15 m s^{-1} for the moist Kelvin mode. Dissipation via radiative and turbulent fluxes and surface stress and friction damps the moist Kelvin mode on a time scale of order 10 days and thus sets a characteristic zonal length scale over which the Kelvin mode may be expected to dominate the teleconnected response. In the equilibrium limit, a substantial zonal temperature gradient develops between the Pacific and remote Tropics; the presence of this gradient is a manifestation of the eastward decay of the ENSO influence away from the Pacific forcing region. We further note that the moist Kelvin wave dynamics implicated in the remote response to abrupt ENSO onset resemble those associated with the Madden–Julian oscillation (MJO) (Knutson and Weickmann 1987).

Figure 3 more concretely demonstrates the linkage between the arrival of the tropospheric temperature anomalies in QTCM1 and the reduction in rainfall and changes to the specific humidity. Within the first 15 days of onset, the tropospheric temperature signal (squares; note that the values plotted correspond to the time at which the time rate of change of tropospheric temperature is maximized) has propagated from the western portion of South America to the eastern Indian Ocean basin. Roughly 1–2 days after the arrival of the temperature wave front, the precipitation anomalies (circles) are maximally suppressed; after a further 1–2 days, the time rate of change of specific humidity (triangles) reaches a maximum. These diagnostics further support the notion that warming-induced convective stabilization reduces precipitation. Moreover, since precipitation removes water vapor from the atmospheric column, the suppression of rainfall leads to increased tropospheric specific humidity.

Although El Niño–related tropospheric temperature anomalies tend to be uniform within the Tropics (Yulaeva and Wallace 1994), spatial inhomogeneities

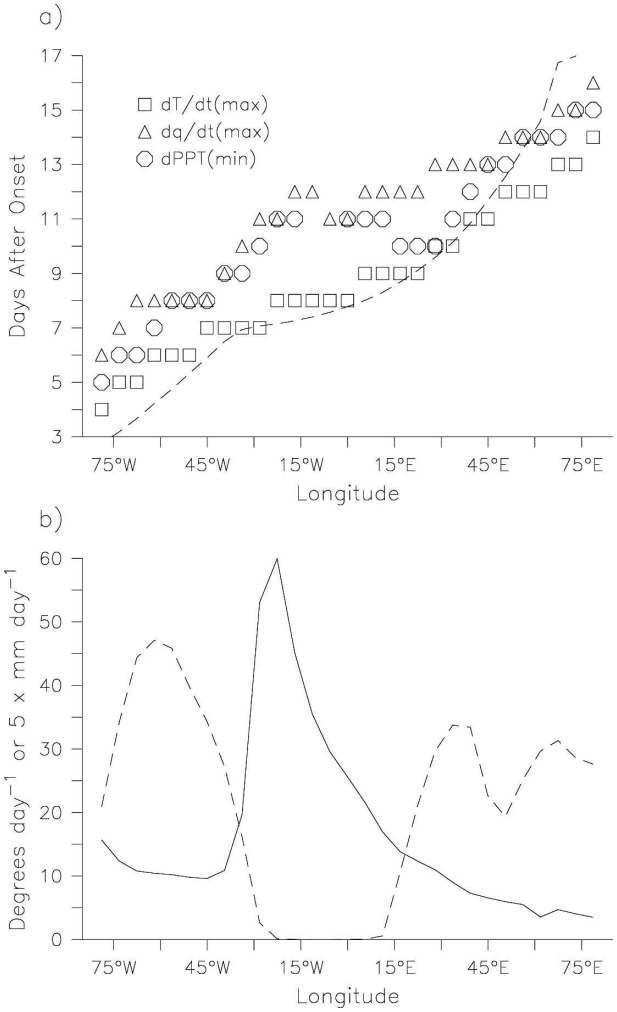

FIG. 3. Zonal propagation of remote tropical climate anomalies in QTCM1. (a) Times (in days following onset) at which the time rates of change of temperature and specific humidity are maximized (squares and triangles) or precipitation is minimized (circles), as a function of longitude and averaged over 10°S–10°N. For comparison, the time at which the temperature anomaly at each longitude reaches 0.2 K is also shown (dashed line). This panel shows the spatiotemporal evolution of fields linked to the initial precipitation decrease, all driven by the initial warm Kelvin wave. (b) The local propagation speed (deg day^{-1}), estimated from the arrival time of the 0.2-K temperature anomaly. The mean precipitation is also shown (mm day^{-1} × 5). These results highlight variations in the Kelvin-like wave speed associated with basic-state climate conditions.

do occur. For example, the CCM3 and QTCM1 temperature snapshots (Figs. 1 and 2) both show a constriction or narrowing of the meridional extent of the temperature anomalies over the Atlantic Ocean. As equilibrium is approached, temperature anomalies in or near this "notch" are of smaller amplitude relative to those downstream over Africa. Another striking example of the inhomogeneous nature of adjustment can be seen in Fig. 3b, which illustrates the longitudinal profile of QTCM1 wave propagation speeds (solid line) estimated from the time required for each longitude to reach 0.2 K (i.e., the dashed line in Fig. 3a). The profile of propagation speeds is characterized by minima over South America and Africa and a maximum over the Atlantic. The distribution of fast and slow wave speeds is broadly consistent with the distribution of near-equatorial mean convection (dashed line); for example, the tropical Atlantic is largely nonconvecting in QTCM1, so the propagation there is essentially governed by dry dynamics and the wave speeds are consequently higher.

4. Interpretation of the initial precipitation suppression

a. Convective scheme sensitivity experiments

QTCM1's Betts–Miller convective parameterization (Betts and Miller 1986) is a convenient starting point for analyzing the initial precipitation behavior. Within the Betts–Miller framework, convective available potential energy (CAPE) and precipitation (proportional to CAPE when CAPE is positive) are obtained from the relaxation of tropospheric temperature to a convective reference temperature profile, T_C:

$$P \propto \Theta(T_C - T)\frac{T_C - T}{\tau_C}, \tag{1}$$

where $\Theta(x)$ is the Heaviside function and τ_C is the convective adjustment time scale (2 h in QTCM1). For fixed T_C, the influence of El Niño on remote precipitation is easily understood, as tropospheric warming would decrease precipitation; however, variations to T_C complicate the response.

Since QTCM1 assumes that deep convection is initiated in the boundary layer, T_C is determined by the boundary layer moist static energy (MSE): to lowest order, the convective reference temperature profile may be regarded as a moist adiabat originating in the boundary layer (Neelin and Zeng 2000); T_C is consequently dependent on boundary layer tropospheric temperature and humidity. Because of the single-mode vertical structure of temperature and humidity, it is possible to cast Eq. (1) in terms of appropriately vertically weighted averages of these quantities; thus, perturbations to the precipitation field anomalies are approximately

$$P' \propto \tilde{q}' - \tilde{T}', \tag{2}$$

where [′] denotes perturbations and [˜] the vertical average appropriate to the convective parameterization.

Equation (2) implicates both temperature and hu-

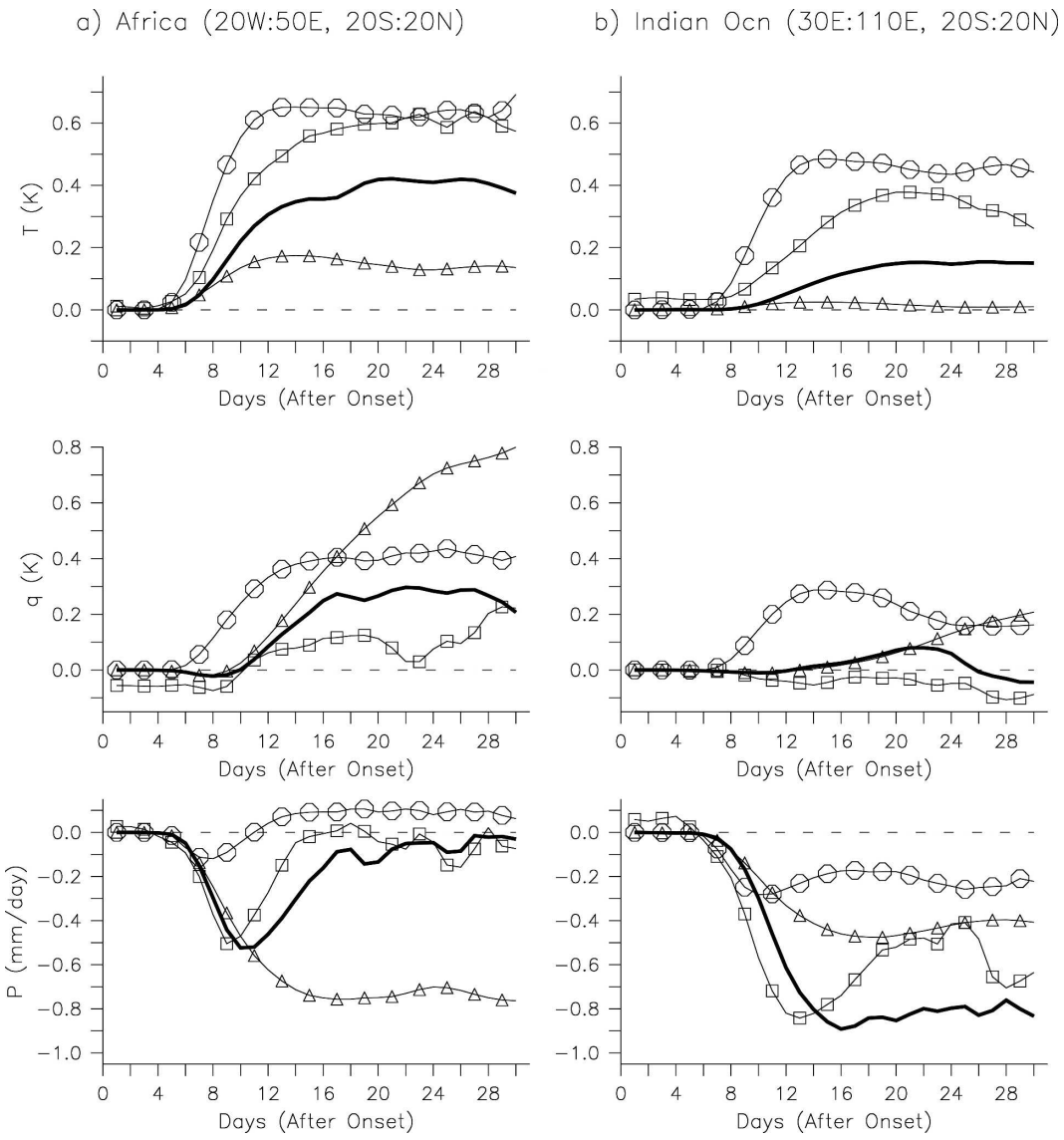

FIG. 4. Remote-averaged anomalies from the standard (thick line), $P(\overline{T})$ (squares), $P(\overline{q})$ (triangles), and $q(\overline{\nabla \cdot \mathbf{v}})$ (circles) QTCM1 El Niño onset simulations. Shown are (a) African and (b) Indian Ocean region (first row) averages of precipitation (mm day^{-1}), and (second row) vertically averaged tropospheric temperature (K) and (third row) specific humidity (K). The results of the sensitivity simulations demonstrate the direct impact of both tropospheric temperature and subsidence in the initial precipitation reduction as well as the subsequent role of moisture feedbacks in modulating the initial response. See sections 4b and 4c for detailed explanations of the sensitivity simulation configurations.

midity in the generation of precipitation anomalies. To explore the roles of temperature and humidity more explicitly, we performed abrupt onset simulations with either the temperature or humidity dependence appearing in the Betts–Miller parameterization constrained to climatology over the remote Tropics; we refer to these sensitivity simulations as "fixed temperature in precipitation" or $P(\overline{T})$ and "fixed humidity in precipitation" or $P(\overline{q})$.

As anticipated, the fixed humidity simulation $P(\overline{q})$ produces an initial precipitation drop following El Niño initiation, as in the standard case (Fig. 4, third row, triangles). Interestingly, the $P(\overline{T})$ simulation also produces initial negative rainfall perturbations (squares); the implication of this is that, initially, both temperature and humidity changes lower precipitation values near the leading edge of the transient wave front. It is only after precipitation decreases that tropospheric specific humidity increases, as is required by the convective QE constraint.

Subsequent to the initial impulse, which occurs at the arrival of the Kelvin-like wave front, the two sensitivity simulations produce distinct time-evolving precipitation signals. Over Africa (Fig. 4a), the $P(\overline{q})$ rainfall remains low, unlike either the standard or $P(\overline{T})$ configurations, in which precipitation more or less recovers to its original level by around day 20. The rapid recovery of tropical African rainfall values in the $P(\overline{T})$ simulation demonstrates the importance of moisture feedbacks to the evolution of the precipitation response: as humidity levels increase, the gap between humidity and temperature in Eq. (2) is decreased, so the stabilizing effect of a warmer troposphere on precipitation is offset. Over the tropical Indian Ocean (Fig. 4b), the $P(\overline{q})$ and $P(\overline{T})$ simulations produce comparable deficits in precipitation (each of which are less than half as large as in the standard simulation) again underscoring the importance of both the humidity and tropospheric temperature effects, although little recovery is evident over the time period plotted.

The sensitivity simulations also suggest a feedback role for the remote tropical precipitation response on the tropospheric temperature and humidity forcing. With a larger remote tropical precipitation reduction, as occurs in the $P(\overline{q})$ simulation over Africa, the tropospheric temperature increase is smaller compared to the standard simulation, while the opposite is true in the $P(\overline{T})$ simulation. Similarly, the relatively larger (land region) precipitation deficit in the $P(\overline{q})$ simulation is associated with higher specific humidity [again with opposing behavior for the $P(\overline{T})$ simulation]. Such results stress that precipitation is not simply passively controlled by temperature and humidity changes but that it modulates these controls as well.

b. *Understanding the remote temperature and humidity forcing*

The rapid propagation of tropospheric temperature anomalies from the tropical Pacific to the remote Tropics is a consequence of the weak Coriolis effect near the equator, which renders the tropical atmosphere unable to maintain strong horizontal temperature gradients (Sobel et al. 2001). Previous studies have argued that the Pacific region convection anomalies dictate the mean level of tropospheric warming to El Niño (Neelin and Held 1987; Yulaeva and Wallace 1994; Sobel et al. 2002; CS02).

In contrast to tropospheric temperature, there is no simple explanation for the remote tropical tropospheric humidity response to El Niño, apart from 1) the thermodynamic tendency for atmospheric humidity to increase with increasing tropospheric temperatures (reflecting both the Clausius–Clapeyron relationship to surface temperature and the QE relationship to tropospheric temperature) and 2) the empirical tendency for the tropical troposphere to maintain fixed relative humidity (Sun and Oort 1995). A strong dynamical determinant of the spatial distribution of humidity anomalies during El Niño is the drying effect associated with wave dynamics, for example, subsidence associated with the passage of the wave front induces vertical moisture divergence in the remote tropical troposphere. We demonstrate the subsidence-related moisture divergence effect through an additional sensitivity simulation, denoted the "fixed subsidence in humidity" or $q(\nabla \cdot \overline{\boldsymbol{v}})$ simulation, in which the remote tropical subsidence field (or equivalently in the framework of QTCM1, the anomalous baroclinic mode divergence $\nabla \cdot \overline{\boldsymbol{v}}$) as it appears in the humidity equation was constrained to climatology. Note that tropospheric temperature was permitted to adjust to changes in remote subsidence field; that is, the relationship between increased subsidence and warming was maintained.

The corresponding response of these simulations for the African and Indian Ocean region averages are shown in Fig. 4 (circles). In contrast to the standard simulation, there is no initial drying of the column (second row) in the $q(\nabla \cdot \overline{\boldsymbol{v}})$ simulation—in fact, the humidity anomalies at the passage of the Kelvin wave are nonnegative—which confirms the initiation of the onset drying by subsidence. Moreover, the remote precipitation field in the $q(\nabla \cdot \overline{\boldsymbol{v}})$ simulation experiences less suppression compared to the standard simulation, despite the fact that the tropospheric temperature anomaly (first row) is larger. These results confirm that it is subsidence—and not other impacts on tropospheric moisture, like anomalous evaporation or horizontal moisture advection—that is responsible for the initial humidity reduction. However, as the teleconnection evolves, feedback-related effects, such as anomalous horizontal moisture advection, may in fact dominate the humidity changes.

c. *Spatial structure of the anomalous remote rainfall response*

The equilibrated climate anomalies of the sensitivity experiments also reveal the roles that temperature and humidity play in determining the spatial distribution of the precipitation response. Figure 5 presents remote regional maps of rainfall anomalies averaged over days 181–240 for the (b) $P(\overline{q})$ and (c) $P(\overline{T})$ simulations as well as (a) the standard case. A striking feature of the $P(\overline{q})$ simulation is how nearly all remote convecting tropical regions (both land and ocean) exhibit a negative precipitation response, mirroring the *initial* response to abrupt onset in the standard simulation. By

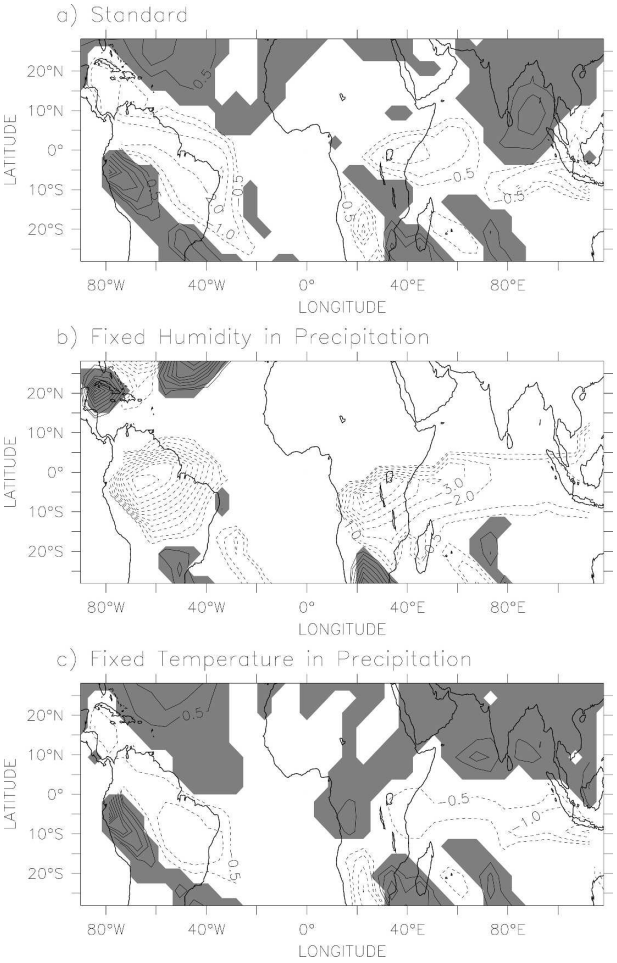

FIG. 5. QTCM1 precipitation anomalies averaged over days 181–240 in the (a) standard, (b) $P(\overline{q})$, and (c) $P(\overline{T})$ simulations. Solid (dashed) contours represent positive (negative) precipitation anomalies, with positive contours shaded for emphasis. The contour interval is 0.25 mm day^{-1} with the zero contour omitted. These results show the relative roles of tropospheric temperature and humidity in determining the equilibrated precipitation response to El Niño.

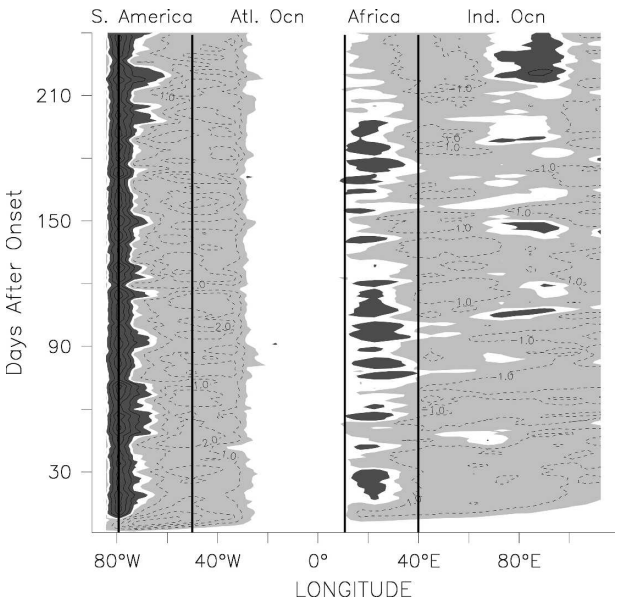

FIG. 6. Hovmoeller plot of QTCM1 precipitation anomalies averaged over 10°S–10°N for the standard abrupt onset simulation. Solid (dashed) contours denote positive (negative) anomalies, with a contour interval of 1 mm day^{-1}. Positive values greater than 0.25 mm day^{-1} (less than −0.25 mm day^{-1}) are shaded dark gray (light gray) for emphasis. The approximate locations of the principal tropical land and ocean regions are also indicated. Note the rapid transition from initially strong negative to positive anomalies over western South America and Africa and the slow transition for the Indian Ocean.

contrast, the spatial characteristics of the equilibrated $P(\overline{T})$ precipitation anomalies resemble those of the standard configuration, although the magnitudes of the $P(\overline{T})$ anomalies are smaller. These results reinforce the notion that humidity changes are critical to the evolution of anomalous remote rainfall to equilibrium, especially in the context of its spatial structure: for example, the humidity changes are integral to the development and maintenance of the localized, positive precipitation anomalies occurring over western South America.

5. The transition of the anomalous remote climate response to equilibrium

Subsequent to the initial drying influence from the Kelvin wave, the remote tropical precipitation response evolves toward a more complex spatial pattern of both positive and negative anomalies, as shown in Fig. 5. A Hovmoeller view of this transition over the equatorial region (Fig. 6) shows clearly that the evolution over land regions (South America and Africa) is essentially complete by day 20, whereas the process tends to be much longer over the Indian Ocean where the initial drying gives way to small positive anomalies after a few months. The difference between (fast) land and (slow) ocean region adjustment suggests that the local surface thermal inertia plays a major role in determining how rapidly a region transitions to equilibrium. The subject of local disequilibrium is explored in this section.

a. Theoretical considerations

The strong vertical coupling between the surface and the atmosphere in the convecting portion of the Tropics is at the heart of the CS02 disequilibrium mechanism: because convection maintains the connection between the surface and the free troposphere, deviations from equilibrium (as induced by El Niño–driven increases to local tropospheric temperature in the single-column model of CS02) cause changes to the convection that act to bring the vertical column back into equilibrium.

As in Neelin and Su (2005), we derive a theoretical expression of the CS02 local disequilibrium starting from the vertically averaged perturbation temperature and moisture equations written in an MSE formulation (see, e.g., Neelin and Zeng 2000):

$$c_A \frac{\partial T'}{\partial t} = -\overline{M}_s \nabla \cdot \boldsymbol{v}' - M_s' \nabla \cdot \overline{\boldsymbol{v}} + R_s' - R_{\mathrm{TOA}}' + H' + P' - T_{\mathrm{adv}}', \quad (3)$$

$$c_A \frac{\partial q'}{\partial t} = \overline{M}_q \nabla \cdot \boldsymbol{v}' + M_q' \nabla \cdot \overline{\boldsymbol{v}} + E' - P' - q_{\mathrm{adv}}', \quad (4)$$

where the notation [$^-$] indicates climatological mean quantities; E, H, R_s, and R_{TOA} are latent, sensible, net surface radiative, and net top-of-the-atmosphere heating, respectively; T_{adv} and q_{adv} are horizontal temperature and moisture advection terms; and M_s and M_q are dry static stability and moisture stratification. Combining (3) and (4) yields an expression for the anomalous divergence $\nabla \cdot \boldsymbol{v}'$; substituting $\nabla \cdot \boldsymbol{v}'$ into (4) and ignoring (for the moment) contributions from T_{adv}', q_{adv}', and $\nabla \cdot \overline{\boldsymbol{v}}$, the moisture equation reduces to

$$P' = E' + m(R_s' + H' + E' - R_{\mathrm{TOA}}') - c_A \frac{\partial}{\partial t}(T + q), \quad (5)$$

with $m = \overline{M}_q(\overline{M}_s - \overline{M}_q)^{-1}$.

As shown in the previous section, for very short times, effectively several days after passage of the Kelvin-like wave front, the anomalous precipitation response is dominated by the atmospheric disequilibrium, represented by the time derivatives on the right-hand side of Eq. (5). At later times, these derivatives become negligible. Further, the sum of the surface fluxes, $R_s' + H' + E'$, is just $-c_m(\partial T_s/\partial t)$. Expanding $E' \approx \varepsilon_H(\gamma T_s' - b_s q')$ and $R_{\mathrm{TOA}}' \approx \varepsilon_R^T T' + \varepsilon_R^q q' + \varepsilon_R^{T_s} T_s'$ (see Neelin and Su 2005 for definitions) and invoking the strict QE limit of $q' \approx nT'$ (with $n \approx 0.7$) allows (5) to be written as

$$P' \approx (\varepsilon_H \gamma - \varepsilon_R^{T_s}) T_s' - m[\varepsilon_R^T + n(\varepsilon_R^q + m^{-1}\varepsilon_H b_s)] \times T' - mc_m \frac{\partial T_s'}{\partial t}, \quad (6)$$

where the contribution from $c_A(\partial/\partial t)$ has been disregarded. The final term on the right-hand side of (6) is the surface disequilibrium term.

For an instantaneous tropospheric warming of magnitude T', the initial surface temperature perturbation is 0 and $-c_m(\partial T_s/\partial t) < 0$. After the surface has equilibrated, on the other hand, there is a finite surface temperature perturbation, which tends to increase P', by the first term on the right-hand side of (6), while the last term vanishes. Thus, the difference between initial and equilibrated precipitation values, considering T' as fixed (so that the middle term on the right-hand side of (6) is identical for all times) is

$$\Delta P' \approx -mc_m \frac{\partial T_s'}{\partial t}(t = 0) - (\varepsilon_H \gamma - \varepsilon_R^{T_s}) T_s' < 0. \quad (7)$$

In other words, the surface disequilibrium effect enhances the precipitation reduction while the net surface flux is nonzero. The time scale for precipitation relaxation to equilibrium depends on the rapidity of the surface temperature adjustment, with shallower mixed layers equilibrating more rapidly. This dependence on the surface thermal inertia is in line with CS02's finding of the local disequilibrium in their single-column-model simulations.

The effect of horizontal temperature and moisture advection, T_{adv}' and q_{adv}', may be quite sizeable, especially regionally (Neelin and Su 2005). These terms may in fact contribute significantly to the temporal evolution of the anomalous remote precipitation response, although the manner in which they do so is nontrivial, since they depend on interactions between circulation and temperature/moisture gradients. The contribution from $\nabla \cdot \overline{\boldsymbol{v}}$, the moisture convergence feedback, is tied to the basic-state circulation: for convergent flow regimes, $\nabla \cdot \overline{\boldsymbol{v}} > 0$, which drives precipitation increases (since humidity increases). Interactions between convergence feedback and moisture advection produce the patterns of negative and positive anomalies observed locally in the remote Tropics.

b. *Adjustment dependence on surface thermal inertia*

To test the role of ocean thermal inertia in the equilibration to ENSO forcing, we performed El Niño onset simulations with the remote ocean mixed layer depth (MLD) varied across a range of values, that is, 4, 12.5, 25, 50, 75, 125, 200, and 500 m. Additionally, a simulation was performed in which the remote ocean SST field was fixed to climatology, which corresponds effectively to infinite MLD. The simulation setup in the varied MLD experiments differs somewhat from the previous QTCM1 simulations: they consist of single integrations rather than ensembles, and mean climate seasonality was not suppressed in these experiments. The peak El Niño forcing was also not introduced instantaneously, although it is still rapid (i.e., 3 months) compared to observed ENSO onset. Such differences, while not inconsequential, do not alter the basic conclusions.

The varied MLD simulations show that the QTCM1 precipitation response over the remote oceans is consistent with the CS02 idea of local disequilibrium (Fig.

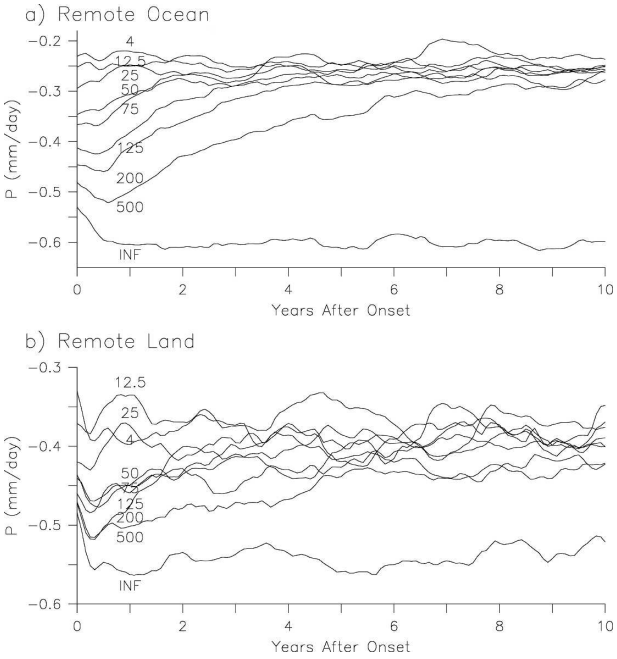

FIG. 7. (a) Remote tropical ocean and (b) land precipitation anomalies (mm day^{-1}) for the QTCM1 varied mixed layer depth experiments. Results shown are for MLDs of 4, 12.5, 25, 50, 75, 125, 200, and 500 m, as well as for fixed SST [or infinite MLD (INF)]. Note that a 12-month running mean has been applied to each time series to reduce the effects of high-frequency variability and seasonality. These panels confirm the role of remote ocean thermal inertia in causing a local disequilibrium response in ocean region precipitation; a nonlocal effect of the ocean thermal inertia is also suggested by MLD-dependent differences in the precipitation transition to equilibrium over remote tropical land regions.

7a). In each MLD simulation, precipitation is suppressed following El Niño onset, with the degree of suppression increasing with increasing remote MLD. All simulations except the fixed SST case eventually equilibrate to a value of roughly -0.25 mm day^{-1} after a few years, with the time scale for adjustment lengthening as MLD increases. By contrast, the fixed SST simulation maintains a nearly constant deficit throughout the duration of the simulation, with a magnitude significantly greater than any of the other simulations. The difference between the infinite MLD precipitation response (-0.6 mm day^{-1}) and the equilibrated response of the finite MLD runs indicates the degree to which the local SST-related disequilibrium contributes to the overall precipitation response: at $\sim$0.35 mm day^{-1}, the magnitude of the disequilibrium effect is larger than the equilibrated anomaly.

c. Mechanism of the thermodynamic SST-related adjustment to equilibrium

Mechanistic insight into the differential response of the precipitation perturbations as MLD is varied can be obtained by considering the full precipitation anomaly budget, analogous to what is often done for surface temperature anomalies (see section 5a):

$$P' \approx \nabla \cdot \overline{\mathbf{v}}(M'_q - mM') + m(R'_s - R'_{\mathrm{TOA}}) + (1+m)E' + mH' - m\left(c_A \frac{\partial T'}{\partial t} + T'_{\mathrm{adv}}\right) - (1+m)\left(c_A \frac{\partial q'}{\partial t} + q'_{\mathrm{adv}}\right). \quad (8)$$

It is instructive to compare the budgets for the two end-member simulations, 4 m and fixed SST, since the former equilibrates rapidly while the latter never reaches equilibrium. Consider the anomalous Indian Ocean precipitation budgets for these simulations (Table 1). Of the six terms on the right-hand side of Eq. (8), the largest difference occurs in the anomalous latent heating component: roughly $\sim$60% of the total Indian Ocean precipitation difference between the 4 m and fixed SST simulations is tied to the difference in evaporation between these two cases; differences in the remaining terms are generally less than ½ as large.

Initially, Indian Ocean latent heating anomalies in both the 4-m MLD and fixed SST simulations are negative, as the ocean–atmosphere-directed latent heat flux falls below climatology and the upper ocean consequently warms. As the remote ocean thermally equilibrates to the imposed El Niño forcing in the 4-m MLD case, the anomalous latent heating contribution to the anomalous precipitation budget reverses sign: approaching equilibrium, anomalous evaporation contributes a cooling tendency that limits further SST increases (see Chiang and Lintner 2005). By contrast, for the fixed SST case, anomalous latent heat flux remains negative throughout the duration of the simulation. The behavior of the budget components highlights potential complexities involved in the budgetary approach, as contributions from some terms compensate or partially offset others.

d. Nonlocal influences on the transition to equilibrium

Although we have emphasized the rapid adjustment of tropical land regions, it is clear from Fig. 7b that the remote land region precipitation anomalies also undergo a slow adjustment, with the adjustment time showing some tendency to increase with increasing MLD. Since the land region surface thermal inertia is unchanged as oceanic MLD is varied, these results imply that the rapidity of the surface thermal response to El Niño over the remote oceans affects rainfall deficits over the remote Tropics as a whole, with a faster ocean

TABLE 1. Indian Ocean anomalous precipitation budgets in the QTCM1 4-m slab ocean and fixed SST simulations. Values in columns 3–5 are in mm day^{-1}. Values in the last column are ratios (expressed as percentages) of the 4 m − fixed SST budget term differences to the total precipitation difference in row 2.

Term		Fixed SST	4 m	4 m − fixed SST	% total
Total precipitation	P'	−0.84	−0.29	0.55	—
Moisture convergence	$\nabla \cdot \bar{\mathbf{v}}(M'_q - mM')$	0.04	0.19	0.15	27
Moisture tendency	$-(c_A(\partial q'/\partial t) + q'_{\text{adv}})(1 + m)$	0.03	−0.13	−0.16	−29
Temperature tendency	$-m[c_A(\partial T'/\partial t) + T'_{\text{adv}}]$	−0.29	−0.35	−0.05	−9
Latent heating	$(1 + m)E'$	−0.20	0.13	0.33	60
Sensible heating	mH'	−0.08	0.03	0.11	20
Net radiative heating	$m(R'_S - R'_{\text{TOA}})$	−0.34	−0.19	0.15	27

thermal response to El Niño reducing anomalous precipitation deficits over remote land regions. The slow adjustment of the ocean mixed layer feeds back onto temperature and humidity; the modulation of these fields is then communicated to remote land regions via wave dynamics, moisture advection, etc. We stress, however, that the nonlocal influence on land region precipitation is manifested mostly by large-scale averages of land region precipitation. On the other hand, the generation of regional-scale features of the anomalous precipitation field, for example, the establishment of positive precipitation anomalies over equatorial western South America and Africa (Fig. 4), occurs relatively rapidly.

6. Summary and conclusions

Using idealized simulations of abrupt El Niño onset, we investigated the adjustment of the remote tropical climate to the abrupt introduction of peak El Niño conditions. The principal findings of our study are as follows.

1) A fast (~10 day) atmospheric adjustment occurs immediately after El Niño onset and is dominated by moist Kelvin-like wave propagation along the equatorial waveguide. The subsidence associated with the Kelvin wave front suppresses remote tropical precipitation by raising tropospheric temperature and reducing humidity. Other potential teleconnection pathways (e.g., forced excitation of extratropical Rossby waves) appear to be less important to the development of the initial response to El Niño conditions in the remote Tropics.
2) After passage of the Kelvin wave front, the remote precipitation deficits generally relax toward smaller equilibrium values as feedback processes modulate the response. These feedbacks are tied to atmospheric humidity anomalies, which (in QTCM1) modify the convective reference temperature profile in the Betts–Miller convective scheme.
3) Remote land region rainfall recovers rapidly from the initial Kelvin wave shock (i.e., within about 10 days), while remote ocean rainfall exhibits a slower relaxation, implying that the underlying surface thermal inertia significantly influences the rapidity of the adjustment process.
4) The transition to equilibrium over remote oceans depends on ocean mixed layer depth, as deepening of the mixed layer leads to less rapid adjustment. In particular, disequilibrium associated with a nonzero net surface flux enhances the precipitation reduction over the remote ocean, in support of the prediction by Chiang and Sobel (2002) of this effect. An anomalous precipitation budget derived from moist static energy balance emphasizes the role of anomalous latent heating in the transition to equilibrium over remote ocean regions.
5) The slow equilibration of the remote ocean also affects the evolution of the areally averaged precipitation anomalies over land, although this nonlocal effect tends to be small.

By itself, the examination of the remote tropical climate adjustment to El Niño conditions does not reveal *why* the remote climate anomalies develop as they do: the determination of the equilibrated state depends ultimately on energy, mass, and momentum constraints. To this end, Su, Neelin, and coworkers (see, e.g., Su and Neelin 2002; Su et al. 2001, 2003, 2005) have developed in great detail a perspective of the ENSO teleconnection based on MSE budgets. The results of these studies typically show that the remote precipitation response satisfies budgetary constraints in regionally distinct and possibly complex ways. As some similarities are clearly evident among or between regions, mechanisms have been advanced to explain such similarities. In general, however, it may not be straightforward to deduce mechanisms based solely on regional MSE budgets, as the MSE budgetary balance may arise from a potentially complex chain of feedbacks.

It is in light of such complexities that we have offered an adjustment-motivated view of the remote ENSO

teleconnection. However, it is worth addressing two deficiencies in our approach. First, with respect to the fast atmosphere-related adjustment, we have not explored in great detail what role atmospheric circulation anomalies may play. Rather, we have focused essentially on thermodynamic considerations (although these are fundamentally inseparable from the dynamics). Regionally, the impact of circulation may be sizeable: the occurrence of localized centers of variability (e.g., the Nordeste region of Brazil) may be tied to changes in circulation, or anomaly–mean field interactions (e.g., mean field advection of anomalous moisture gradients).

Second, with respect to the longer time-scale adjustment, we have only considered ocean thermal inertia effects, although it is clear that in reality ocean dynamical effects may play a substantial, if not leading, role in mediating the adjustment to El Niño forcing. Our decision to focus here on thermal effects is a result of expediency; it is a simpler problem, and there exists some basis (e.g., CS02) on how to view the ocean thermal adjustment, particularly with respect to precipitation. Ocean dynamical effects likely operate on time scales long enough to render our examination of the transition to equilibrium incomplete (at best) or unrealistic (at worst); however, ocean thermal effects *must* be operating at some level in the real world—we would argue based on the results presented here that the thermal adjustment contribution is nonnegligible—and for that reason it is valuable to look at this problem.

Of course, it is also of interest to determine whether any elements of the observed ENSO teleconnection may be viewed more accurately in an adjustment paradigm, as opposed to a more or less equilibrated one. Fast adjustment signals as described here are unlikely to be discernible in the observations, given the slow time evolution of ENSO events and the inherent noisiness of the atmosphere, although the similarities to the MJO are worth exploring. However, the longer timescale adjustment associated with the thermal equilibration of the ocean mixed layer may be more readily detected in the observations. For a realistic MLD (say 50 m), the difference in precipitation amplitude between the initial and equilibrated phases is ~30%. Further, the adjustment time scale is ~1 yr, which is comparable to the duration of a typical ENSO event. Still, identification of the ocean–atmosphere disequilibrium-related adjustment effects may be complicated by (or even small relative to) ocean dynamical effects, not to mention that seasonality may further complicate the observational analyses. The most likely periods in the evolution of ENSO events where adjustment effects may be seen are during fast transitions of the ENSO state. We note that observed *decays* from peak El Niño conditions to neutral or even La Niña states are typically faster than development phases; it may therefore be worthwhile to consider the impact of adjustment during El Niño decay.

Acknowledgments. The authors thank Inez Fung, J. David Neelin, Jian Lu, Chris Holloway, and two anonymous reviewers for insightful, thought-provoking comments and J. David Neelin, Matt Munnich, and Hui Su for use of and computational assistance with QTCM1. The CCM3 simulations were executed on an IBM-SP maintained by the Scientific Computing Division at NCAR. Funding was provided by NOAA CLIVAR-Pacific Grant NA03OAR4310066. BRL also acknowledges partial support from NOAA Grant NA05OAR4311134 (J. David Neelin, P.I.).

REFERENCES

Alexander, M. A., and Coauthors, 2002: The atmospheric bridge: The influence of ENSO teleconnections on air–sea interaction over the global oceans. *J. Climate,* **15,** 2205–2231.

Betts, A. K., and M. J. Miller, 1986: A new convective adjustment scheme. 2. Single column tests using GATE Wave, BOMEX, ATEX and arctic air-mass data sets. *Quart. J. Roy. Meteor. Soc.,* **112,** 693–709.

Bonan, G. B., 1998: The land surface climatology of the NCAR Land Surface Model coupled to the NCAR Community Climate Model. *J. Climate,* **11,** 1307–1325.

Chiang, J. C. H., and A. H. Sobel, 2002: Tropical tropospheric temperature variations caused by ENSO and their influence on the remote tropical climate. *J. Climate,* **15,** 2616–2631.

——, and B. R. Lintner, 2005: Mechanisms of remote tropical surface warming during El Niño. *J. Climate,* **18,** 4130–4149.

——, M. Biasutti, and D. S. Battisti, 2003: Sensitivity of the Atlantic intertropical convergence zone to Last Glacial Maximum boundary conditions. *Paleoceanography,* **18,** 1094, doi:10.1029/2003PA000916.

Chou, C., and J. D. Neelin, 2004: Mechanisms of global warming impacts on regional tropical precipitation. *J. Climate,* **17,** 2688–2701.

——, ——, and H. Su, 2001: Ocean–atmosphere–land feedbacks in an idealized monsoon. *Quart. J. Roy. Meteor. Soc.,* **127,** 1869–1891.

Frierson, D. M. W., 2007: Convectively coupled Kelvin waves in an idealized moist general circulation model. *J. Atmos. Sci.,* **64,** 2076–2090.

Giannini, A., and Coauthors, 2001: The ENSO teleconnection to the tropical Atlantic Ocean: Contributions of the remote and local SSTs to rainfall variability in the tropical Americas. *J. Climate,* **14,** 4530–4544.

Gill, A. E., 1980: Some simple solutions for heat-induced tropical circulation. *Quart. J. Roy. Meteor. Soc.,* **106,** 447–462.

——, 1982a: *Atmosphere–Ocean Dynamics*. Academic Press, 662 pp.

——, 1982b: Studies of moisture effects in simple atmospheric models: The stable case. *Astrophys. Fluid Dyn.,* **19,** 119–152.

Hales, K., J. D. Neelin, and N. Zeng, 2004: Sensitivity of tropical land climate to leaf area index: Role of surface conductance versus albedo. *J. Climate,* **17,** 1459–1473.

Heckley, W. A., and A. E. Gill, 1984: Some simple analytic solutions to the problem of forced equatorial long waves. *Quart. J. Roy. Meteor. Soc.,* **110,** 203–217.

Kalnay, E., and Coauthors, 1996: The NCEP/NCAR 40-Year Reanalysis Project. *Bull. Amer. Meteor. Soc.,* **77,** 437–471.

Kidson, J. W., 1975: Tropical eigenvector analysis and Southern Oscillation. *Mon. Wea. Rev.,* **103,** 187–196.

Kiehl, J. T., and Coauthors, 1998: The National Center for Atmospheric Research Community Climate Model: CCM3. *J. Climate,* **11,** 1131–1149.

Klein, S. A., B. J. Soden, and N. C. Lau, 1999: Remote sea surface temperature variations during ENSO: Evidence for a tropical atmospheric bridge. *J. Climate,* **12,** 917–932.

Knutson, T. R., and K. M. Weickmann, 1987: 30–60 day atmospheric oscillations: Composite life cycles of convection and circulation anomalies. *Mon. Wea. Rev.,* **115,** 1407–1436.

Lau, N. C., and M. J. Nath, 1996: The role of the "atmospheric bridge" in linking tropical Pacific ENSO events to extratropical SST anomalies. *J. Climate,* **9,** 2036–2057.

Lintner, B. R., and J. C. H. Chiang, 2005: Reorganization of tropical climate during El Nino: A weak temperature gradient approach. *J. Climate,* **18,** 5312–5329.

Nakajima, K., and Coauthors, 2004: Initial development of tropical precipitation in response to a local warm SST area: An aqua-planet ensemble study. *J. Meteor. Soc. Japan,* **82,** 1483–1504.

Neelin, J. D., and I. M. Held, 1987: Modeling tropical convergence based on the moist static energy budget. *Mon. Wea. Rev.,* **115,** 3–12.

——, and J.-Y. Yu, 1994: Modes of tropical variability under convective adjustment and the Madden–Julian oscillation. Part I: Analytical theory. *J. Atmos. Sci.,* **51,** 1876–1894.

——, and N. Zeng, 2000: A quasi-equilibrium tropical circulation model—Formulation. *J. Atmos. Sci.,* **57,** 1741–1766.

——, and C. Chou, 2004: Mechanisms of global warming impacts on regional tropical precipitation. *J. Climate,* **17,** 2688–2701.

——, and H. Su, 2005: Moist teleconnection mechanisms for the tropical South American and Atlantic sector. *J. Climate,* **18,** 3928–3950.

——, C. Chou, and H. Su, 2003: Tropical drought regions in global warming and El Nino teleconnections. *Geophys. Res. Lett.,* **30,** 2275, doi:10.1029/2003GL018625.

Saravanan, R., and P. Chang, 2000: Interactions between tropical Atlantic variability and El Niño–Southern Oscillation. *J. Climate,* **13,** 2177–2194.

Sobel, A. H., J. Nilsson, and L. M. Polvani, 2001: The weak temperature gradient approximation and balanced tropical moisture waves. *J. Atmos. Sci.,* **58,** 3650–3665.

——, I. M. Held, and C. S. Bretherton, 2002: The ENSO signal in tropical tropospheric temperature. *J. Climate,* **15,** 2702–2706.

Su, H., and J. D. Neelin, 2002: Teleconnection mechanisms for tropical Pacific descent anomalies during El Niño. *J. Atmos. Sci.,* **59,** 2694–2712.

——, ——, and C. Chou, 2001: Tropical teleconnection and local response to SST anomalies during the 1997-1998 El Niño. *J. Geophys. Res.,* **106,** 20 025–20 043.

——, ——, and J. E. Meyerson, 2003: Sensitivity of tropical tropospheric temperature to sea surface temperature forcing. *J. Climate,* **16,** 1283–1301.

——, ——, and ——, 2005: Mechanisms for lagged atmospheric response to ENSO forcing. *J. Climate,* **18,** 4195–4215.

Sun, D.-Z., and A. H. Oort, 1995: Humidity–temperature relationships in the tropical troposphere. *J. Climate,* **8,** 1974–1987.

Tang, B. H., and J. D. Neelin, 2004: ENSO influence on Atlantic hurricanes via tropospheric warming. *Geophys. Res. Lett.,* **31,** L24204, doi:10.1029/2004GL021072.

Yulaeva, E., and J. M. Wallace, 1994: The signature of ENSO in global temperature and precipitation fields derived from the Microwave Sounding Unit. *J. Climate,* **7,** 1719–1736.

Zeng, N., and J. D. Neelin, 1999: A land–atmosphere interaction theory for the tropical deforestation problem. *J. Climate,* **12,** 857–872.

——, and ——, 2000: The role of vegetation–climate interaction and interannual variability in shaping the African savanna. *J. Climate,* **13,** 2665–2670.

——, ——, K. M. Lau, and C. J. Tucker, 1999: Enhancement of interdecadal climate variability in the Sahel by vegetation interaction. *Science,* **286,** 1537–1540.

——, ——, and C. Chou, 2000: A quasi-equilibrium tropical circulation model—Implementation and simulation. *J. Atmos. Sci.,* **57,** 1767–1796.